

**Seismic interferometry facilitating the imaging of shallow shear-wave reflections hidden beneath surface waves**

Liu, Jianhuan; Draganov, Deyan; Ghose, Ranajit

**DOI**

[10.3997/1873-0604.2018013](https://doi.org/10.3997/1873-0604.2018013)

**Publication date**

2018

**Document Version**

Accepted author manuscript

**Published in**

Near Surface Geophysics

**Citation (APA)**

Liu, J., Draganov, D., & Ghose, R. (2018). Seismic interferometry facilitating the imaging of shallow shear-wave reflections hidden beneath surface waves. *Near Surface Geophysics*, 16(3), 372-382. <https://doi.org/10.3997/1873-0604.2018013>

**Important note**

To cite this publication, please use the final published version (if applicable). Please check the document version above.

**Copyright**

Other than for strictly personal use, it is not permitted to download, forward or distribute the text or part of it, without the consent of the author(s) and/or copyright holder(s), unless the work is under an open content license such as Creative Commons.

**Takedown policy**

Please contact us and provide details if you believe this document breaches copyrights. We will remove access to the work immediately and investigate your claim.

# 1 Seismic interferometry facilitating the imaging of shallow 2 shear-wave reflections hidden beneath surface waves

3  
4 *Jianhuan Liu<sup>1</sup>, Deyan Draganov<sup>1</sup>, Ranajit Ghose<sup>1</sup>*

5 *<sup>1</sup>Department of Geoscience and Engineering, Delft University of Technology, The*  
6 *Netherlands. Email: [j.liu-4@tudelft.nl](mailto:j.liu-4@tudelft.nl); [d.s.draganov@tudelft.nl](mailto:d.s.draganov@tudelft.nl); [r.ghose@tudelft.nl](mailto:r.ghose@tudelft.nl)*

7  
8 *Received September 2017, revision accepted April 2018*

## 9 10 11 12 **Abstract**

13 High-resolution reflection seismics is a powerful tool that can provide the required  
14 resolution for subsurface imaging and monitoring in urban settings. Shallow seismic  
15 reflection data acquired in soil-covered sites are often contaminated by source-coherent  
16 surface waves and other linear moveout noises (LMON) that might be caused by, e.g.,  
17 anthropogenic sources or harmonic distortion in vibroseis data. In the case of shear-wave  
18 seismic reflection data, such noises are particularly problematic as they overlap the useful  
19 shallow reflections. We have developed new schemes for suppressing such surface-wave  
20 noise and LMON while still preserving shallow reflections, which are of great interest to  
21 high-resolution near-surface imaging. We do this by making use of two techniques. First,  
22 we make use of seismic interferometry to retrieve predominantly source-coherent surface  
23 waves and LMON. We then adaptively subtract these dominant source-coherent surface  
24 waves and LMON from the seismic data in a separate step. We illustrate our proposed  
25 method using synthetic and field data. We compare results from our method with results  
26 from frequency–wavenumber (f-k) filtering. Using synthetic data, we show that our  
27 schemes are robust in separating shallow reflections from source-coherent surface waves  
28 and LMON even when they share very similar velocity and frequency contents, whereas  
29 f-k filtering might cause undesirable artefacts. Using a field shear-wave reflection dataset

30 characterised by overwhelming LMON, we show that the reflectors at a very shallow  
31 depth can be imaged because of significant suppression of the LMON due to the  
32 application of the scheme that we have developed.

33

## 34 **Introduction**

35 Engineering and environmental problems (e.g., sinkhole and groundwater-related issues)  
36 in urban areas often require highly detailed information about the subsurface structure in  
37 depth to a few metres. Among all available geophysical methods, for soil-covered areas,  
38 high-resolution reflection seismics using shear or S-waves (e.g., Pullan, Hunter and  
39 Neave 1990; Hasbrouck 1991; Ghose, Brouwer and Nijhof 1996; Ghose and Goudswaard  
40 2004; Pugin *et al.* 2004; Krawczyk, Polom and Beilecke 2013; Konstantaki *et al.* 2014)  
41 is one of the few options to accomplish the target resolution of the subsurface in an urban  
42 setting. For example, using specialised seismic vibratory sources and shear waves, it has  
43 been possible in the past to achieve decimetre-scale seismic resolution in the near-surface  
44 soils (e.g., Ghose *et al.* 1996; Brouwer *et al.* 1997; Ghose *et al.*, 1998; Ghose 2002; Ghose  
45 and Goudswaard 2004).

46       However, most cities are located in soil-covered plains or Quaternary basins  
47 overlying consolidated bedrock ( Sinsakul 2000; Haworth 2003). Shallow shear-wave  
48 reflection data acquired in such soil-covered sites is characterised by large amount of  
49 (dispersive) surface waves, which generally camouflage the very shallow reflections. The  
50 conventional techniques for suppression of surface waves, e.g., muting or spatial filtering  
51 (Yilmaz 2001) are ineffective or even detrimental to the target reflections in suppressing  
52 this source-generated noise, especially at near offsets. This is especially challenging in  
53 urban settings where the available source-receiver offset is often quite limited, and the

54 velocity and frequency content of the surface waves largely overlap with those of the  
55 target shear-wave reflections (unlike compressional wave reflections, which usually have  
56 much higher velocities than the surface waves). The first goal of the present research is,  
57 therefore, to reduce the surface waves due to the active source (source-coherent surface  
58 waves) and reveal the very shallow reflections in the recorded data using seismic  
59 interferometry (SI) and adaptive subtraction (AS).

60         Also, human activities (e.g., near-by traffic, construction works, or movement of  
61 people) are common during urban seismic surveys. When many such noise sources are  
62 excited simultaneously in the crossline direction, the traveltime from these noise sources  
63 to all receivers depends on the distance between these sources and the receivers. In the  
64 urban settings, such noise sources are mainly linearly distributed (such as in construction  
65 works or for moving vehicles), which means that the traveltime of such noise recorded in  
66 the shot gather will have a linear moveout. These arrivals exacerbate the already difficult  
67 problem of removing the surface waves generated by the active source used in the seismic  
68 survey. The source-incoherent surface waves can result in lower resolution in the imaging  
69 results and even lead to wrong seismic interpretation. The second motivation of the  
70 present study is to remove such source-incoherent surface waves using new processing  
71 schemes that we developed.

72         In this paper, we first present the steps for the implementation of our method. We  
73 then demonstrate the feasibility of our method in suppressing surface waves (from both  
74 inline and crossline directions) through modelling studies. Finally, we implement this  
75 method on a field dataset that is heavily contaminated by such noises.

76

## 77 **Methodology**

78 In our proposed method, we make use of SI to retrieve, at first, the dominant surface  
79 waves. The retrieved surface-wave energy is then adaptively subtracted from the data.  
80 For the horizontal arrivals (or dipping arrivals), they are retrieved at both causal and  
81 acausal time. Hence, they need to be isolated from the retrieved data in order to be further  
82 shifted back to the position of the physical arrivals, this is done by using singular value  
83 decomposition (SVD) filtering (for dipping arrivals, this involves linear move out  
84 correlation (LMO), SVD, and then inverse LMO). In this section, we first state how to  
85 implement seismic interferometry, adaptive subtraction, and SVD filtering separately.  
86 Then, a workflow is presented to describe how to assemble the separate operations to  
87 suppress different types of surface waves.

88

## 89 **Seismic interferometry**

90 SI refers to the process of estimating the full Green's functions (GF) between two  
91 receivers, by cross-correlating the recordings at the two receivers and stacking the  
92 crosscorrelations for all the sources (Wapenaar and Fokkema 2006). For the urban  
93 seismic survey using active sources, the retrieved GF  $\hat{G}(\mathbf{X}_A, \mathbf{X}_B, \omega)$  between two  
94 receivers at  $\mathbf{X}_A$  and  $\mathbf{X}_B$  can be determined by (Halliday *et al.* 2007):

$$95 \hat{G}(\mathbf{X}_A, \mathbf{X}_B, \omega) + \hat{G}^*(\mathbf{X}_A, \mathbf{X}_B, \omega) \approx \sum_{n=1}^N \hat{G}^*(\mathbf{X}_B, \mathbf{X}_i, \omega) \hat{G}(\mathbf{X}_A, \mathbf{X}_i, \omega) \Delta \mathbf{X}_i, \quad (1)$$

96 where  $\hat{G}(\mathbf{X}_B, \mathbf{X}_i, \omega)$  is a recording at receiver  $\mathbf{X}_B$  from a source at  $\mathbf{X}_i$  ( $\hat{G}(\mathbf{X}_A, \mathbf{X}_i, \omega)$  is  
97 similar) represented in the frequency domain as indicated by the hat above  $G$ ; the asterisk  
98 (\*) denotes the complex conjugation in the frequency domain, which corresponds to time-  
99 reversal in the time domain.  $N$  represents the number of active sources. If the sources  
100 were impulses,  $\hat{G}$  would have represented an impulse response. For transient sources,  $\hat{G}$   
101 would represent a pressure or a particle-velocity recording convolved with the

102 autocorrelation of the source's time function. Via formula (1), we can turn the receiver at  
103  $\mathbf{X}_B$  into a virtual source. If we keep the receiver at  $\mathbf{X}_B$  fixed and repeat the correlation and  
104 summation process for all the other receivers, the resulting retrieved result can  
105 approximate a virtual common-source gather with a virtual source located at  $\mathbf{X}_B$ . The  
106 theory of SI requires that the sources effectively surround the receivers and illuminate  
107 them homogeneously (Wapenaar and Fokkema 2006). When the receivers are at the  
108 surface, i.e.,  $\hat{G}$  represents a particle-velocity recording, active sources are required only  
109 in the subsurface (Wapenaar and Fokkema 2006). For the usual seismic exploration  
110 survey, e.g., for near-surface imaging, the active sources are present at the surface, where  
111 they are not required. Because of that, the retrieved result would contain physical arrivals  
112 – the direct and surface waves, but also pseudo-physical reflections and non-physical  
113 arrivals (e.g., Mikesell *et al.* 2009; Draganov, Heller, and Ghose 2012; King and Curtis  
114 2012; Draganov *et al.* 2013). For a line survey, as all active sources are at the surface,  
115 they all will contribute to the retrieval of the direct and surface waves because all of them  
116 fall into the so-called stationary phase region (Snieder 2004). In this way, the result  
117 retrieved by SI will be dominated by surface waves, as they are the most energetic arrivals  
118 in a recording from active sources at the surface.

119

## 120 **Adaptive subtraction**

121 We use Figure 1 to illustrate the basic principles of AS. Figure 1a can be considered as a  
122 simple seismic data that consists of four events: one weak reflection at 100 ms, and  
123 another three high-amplitude surface-wave arrivals at 200 ms, 300 ms, and 400 ms,  
124 respectively. Figure 1b corresponds exactly to the surface-wave part of Figure 1a. By  
125 minimizing the difference between Figure 1a and Figure 1b, the surface waves in Figure

126 1a can be suppressed. This is done by estimating a shaping filter  $\mathbf{f}$ , that can minimise the  
127 following objective function:

$$128 \quad \mathbf{D}^{refl} = |\mathbf{D} - \mathbf{f}\mathbf{D}^{sw}|_{min}, \quad (2)$$

129 where  $\mathbf{D}$  is the raw data (Figure 1a),  $\mathbf{D}^{sw}$  contains the surface-wave part of  $\mathbf{D}$  (Figure 1b),  
130 and  $\mathbf{D}^{refl}$  (Figure 1d) represents the data after suppression of the surface waves. We obtain  
131 this shaping filter  $\mathbf{f}$  using the L1-norm, which follows the approach proposed by Guitton  
132 and Verschuur (2004). The convolution between the estimated shaping filter  $\mathbf{f}$  and  $\mathbf{D}^{sw}$   
133 (Figure 1b) leads to  $\mathbf{f}\mathbf{D}^{sw}$  (Figure 1c), which will then be directly subtracted from  $\mathbf{D}$   
134 (Figure 1a), as expressed in equation (2), giving Figure 1d. Comparing Figure 1a and  
135 Figure 1d, we can see that the strong surface waves have been greatly reduced in Figure  
136 1d, while the weak reflection at 100 ms is preserved.

137 In a field seismic reflection experiment, the exact location of surface waves  
138 recorded in the data (as in Figure 1b) are unknown. However, SI has proven to be a robust  
139 tool for estimating the surface-wave energy between receivers under certain survey  
140 geometry (e.g., Dong, He, and Schuster 2006; Halliday *et al.* 2007; Konstantaki *et al.*  
141 2015). This means that the retrieved surface waves can then be regarded as an input for  
142 AS (as in Figure 1b), which will be adaptively subtracted from the data (as in Figure 1a).

143

## 144 **SVD filtering**

145 Multi-trace seismic data can be represented as a matrix  $\mathbf{C}$  of size  $(m \times n)$ , where  $\mathbf{m}$  denotes  
146 traces number and  $\mathbf{n}$  denotes time samples. The SVD of matrix  $\mathbf{C}$  is the factorization of  
147  $\mathbf{C}$  into the product of three matrices (Golub and van Loan 1996; Melo *et al.* 2013), which  
148 is  $\mathbf{C}=\mathbf{U}\mathbf{S}\mathbf{V}^t$ , where  $\mathbf{U}$  and  $\mathbf{V}$  are the orthonormal left and right singular vectors, and matrix  
149  $\mathbf{S}$  is a diagonal matrix composed of the singular values of the original matrix  $\mathbf{C}$ , in

150 descending order. By taking only the contribution of the first  $j$  singular values from  $\mathbf{C}$ , a  
151 lower-rank approximation of  $\mathbf{C}$  is obtained as:  $\mathbf{C}_j = \mathbf{U}\mathbf{S}_j\mathbf{V}^t$  (Eckart and Young 1936).  
152 Figure 2 illustrates how matrix  $\mathbf{C}$  is approximated by its lower-rank matrix  $\mathbf{C}_j$ . Since SVD  
153 is a coherency-based technique (Bekara and van der Baan 2007), for the horizontal  
154 arrivals in Figure 2a, which show a high degree of coherency across the traces, they can  
155 be nicely isolated from the data by setting  $j$  to 2 (Figure 2d).

156

### 157 **Modelling study 1: suppression of source-coherent surface waves**

158 In Figure 3, we present the flowchart of the scheme for implementing SI+AS. Next, to  
159 demonstrate the effectiveness of SI+AS in the removal of different types of surface waves,  
160 which we typically confront in data from urban sites (where high-resolution seismic  
161 imaging is often of great value), we perform synthetic modelling studies. We consider a  
162 four-layer model (Figure 4). A 3-layered partially saturated top soil of total thickness of  
163 12 m overlies the fully saturated soil below. We use an elastic finite-difference modelling  
164 scheme to generate synthetic common-source gathers (Thorbecke and Draganov 2011).  
165 The first source is positioned at 0 m and the last one at 30 m; the source spacing is 1 m.  
166 The array of receivers starts at 6 m and ends at 23.5 m, with a spacing between receivers  
167 of 0.5 m. Following the criteria of stability and numerical dispersion, we set the spatial  
168 grid of the model at 0.1 m and the time step of the modelling at 0.02 ms. To model shear  
169 wave, which we generated and recorded in the field data, the sources are excited along  
170 the inline direction and the vertical component of the data are used. The source signature  
171 is a 90-Hz Ricker wavelet. To suppress the reflections from the bottom and the side  
172 boundaries during the numerical modelling, we implement absorbing boundary  
173 conditions for these boundaries with a taper of 100 points.

174           Figure 5a shows an example of synthetic shot gathers for the source positioned at  
175   15 m along the horizontal direction of the survey line. The surface waves, especially at  
176   far offset (see red ellipse in Figure 5a), mask the useful reflections. To reveal these  
177   reflections, we first make use of SI to retrieve a virtual common-source gather for a  
178   receiver located at 15 m (this receiver becomes the virtual source), following the steps  
179   described earlier in the methodology section. As shown in Figure 5b, the dominant  
180   surface waves in Figure 5a are retrieved well, while the retrieved reflections are  
181   significantly suppressed. We then adaptively subtract Figure 5b from Figure 5a, which  
182   results in Figure 5c. We analyse this result in Figure 6c, by comparing it with the data  
183   after conventional frequency-wavenumber (f-k) filtering (Figure 6b). We also show a  
184   reference shot gather (Figure 6d) without surface waves, modelled by replacing the free  
185   surface by a homogenous half space, to verify the effectiveness of these two techniques.  
186   As can be seen in Figure 6c, SI+AS does well in suppressing surface waves and hence  
187   two reflections with moveouts similar to the true reflections in Figure 6d can now be  
188   easily identified. For the used simple model, the f-k filtering also delivers good results  
189   and these two reflections can also be identified in Figure 6b; however, to avoid filtering  
190   out the reflection from the interface at 7 m, some surface-wave energy still leaked through  
191   the filter, as can be seen above that reflection.

192           To pick root-mean-square (RMS) velocities for stacking, we then carry out  
193   analysis using constant velocity stack (CVS) in the common midpoint (CMP) domain for  
194   the raw data, for the data after f-k filtering, and for the data after SI+AS. A selected  
195   representative part of the constant velocity stacked section is displayed in Figure 7.  
196   Because the surfaces waves present in the modelled data are characterized by moveout  
197   velocities similar to those of the useful reflection events, the alignment in the panels in

198 Figure 7a is ambiguous, making the picking of velocities inaccurate. Such ambiguity is  
199 significantly reduced in Figure 7b, which shows CVS of the same data after f-k filtering.  
200 As is shown in Figure 7b, the first event is flat in the first panel, while the second event  
201 in third panel. Figure 7c is the CVS of this data after SI+AS. Comparing Figure 7b and  
202 Figure 7c, we find that they both offer the same ease for picking the RMS velocity (0 ms-  
203 170 m/s; 68 ms-210 m/s); these velocities will be used in the following stacking procedure.  
204 However, Figure 7c shows a higher signal/noise ratio (S/N), when inspected carefully  
205 (e.g., the blue ellipse). We will further compare in the stacked section this effectiveness  
206 of suppressing different types of surface waves using f-k filtering and SI+AS schemes.

207 Figure 8a shows the stacked section obtained from the raw (unfiltered) active-  
208 source data. In this stacked section, the inclined, high-amplitude surface waves (as the  
209 one marked by the red ellipse) overlap the shallow shear-wave reflectors, making it  
210 difficult to identify the latter in this area. However, due to the effective removal of the  
211 surface waves by the application of SI+AS, in the resulting stacked section, shown in  
212 Figure 8c, these same reflectors (red arrows) are much more continuous and clearer, and  
213 thus quite easy to interpret. These reflectors are also correctly imaged in the stacked  
214 section after f-k filtering, as is shown in Figure 8b. However, due to the close overlap  
215 between surface waves and reflections in the f-k domain, it is difficult to design the f-k  
216 filtering parameters to suppress sufficiently the surface waves. This leads to some leakage  
217 of surface waves at certain shots. The artefacts in Figure 8b (see the red ellipse) are caused  
218 by stacking of such leaked surface-wave energy. Note that the results in Figure 8b and 8c  
219 exhibit apparent curving of the reflector at 7 m and lower amplitude of the reflector at 12  
220 m on the left and right sides. This is caused by reduced stacking power in the CMP gathers  
221 at those positions.

222

223 **Modelling study 2: suppression of source-coherent surface waves and**  
224 **horizontal LMON**

225 When conducting seismic surveys in urban environments, often, the recorded data contain  
226 surface waves that are not connected to the active source used in the survey. Such surface  
227 waves could be due to construction work, traffic passing close to the survey site, walking  
228 people, etc. These surface waves most likely would not be aligned with the survey line,  
229 but would be propagating in a crossline direction. This kind of surface-wave energy,  
230 unlike the surface waves generated by the active sources that we have discussed in the  
231 previous section, can be retrieved by the application of SI at times that are different from  
232 the times in the original active-source data, i.e., they will result in the retrieval of non-  
233 physical arrivals. Hence, such source-incoherent surface waves are hard to suppress from  
234 the original data using the procedure described above. Therefore, we consider a new  
235 approach to suppress this type of noise with the aim to make the previous SI+AS scheme  
236 work also in this situation.

237 When the noise source that generates the crossline surface waves is moving  
238 parallel to the survey line (e.g., from traffic passing by), and when the noise source is not  
239 too close to the receivers, the traveltimes from the noise source to each receiver is almost  
240 the same. These arrivals will be characterized by nearly horizontal moveouts. To simulate  
241 this situation, we add surface waves with horizontal moveouts to our previously modelled  
242 data. In Figure 9a, we show an example of the resulting synthetic shot gather and mark  
243 areas containing this type of surface-wave energy by blue arrows. Figure 9b illustrates  
244 the result of the application of SI. We can see the dominant, retrieved non-physical  
245 surface-wave arrivals at both causal and acausal times – the horizontal arrivals at 0 ms

246 and at about +/- 100 ms. The other dominant, retrieved arrival is the source-coherent  
247 surface wave. Concentrating on the horizontal surface waves, we can see that in Figure  
248 9b the horizontal arrivals (marked by blue arrows) are retrieved, but at times not  
249 coinciding with the times in the original data. This happens as the SI process effectively  
250 eliminates the common travel path shared by the two arrivals recorded at the two receivers.  
251 The SI process "recognizes" the earlier horizontal surface wave in Figure 9a as the arrival  
252 bearing the common travel path, and eliminates its time from the time of the later  
253 horizontal surface wave. To approximate both horizontal surface waves in Figure 9a as  
254 good as possible, we first apply SVD filtering to isolate them from the rest of the retrieved  
255 arrivals. We then use the acausal part of the isolated horizontal arrivals and shift them  
256 back to the physical time of the original horizontal surface waves in Figure 9a, which  
257 results in Figure 9c. The shifting is currently performed manually, but this process could  
258 be automated (beyond the scope of this work). We use the acausal part as it is free from  
259 interference from other arrivals. Looking at the retrieved inline surface waves (red arrow  
260 in Figure 9b), we see that its arrival time is consistent with the time of the original inline  
261 surface wave in Figure 9a (as should be expected from what was shown in the modelling  
262 study 1). For this retrieved arrival, we only need to isolate it from Figure 9b by subtracting  
263 the full isolated horizontal arrivals from Figure 9b and then taking the causal part of the  
264 result, which gives Figure 9d. Finally, these retrieved dominant arrivals (Figure 9c and  
265 Figure 9d) can now be adaptively subtracted one after the other from the original gather  
266 (Figure 9a), resulting in Figure 9e.

267 We also apply f-k filtering to Figure 9a in an attempt to suppress the inline surface  
268 waves and horizontal arrivals, the result of which is shown in Figure 10b. Comparing  
269 Figure 10b and Figure 10d, we see that two reflections can now be identified (red arrows

270 in Figure 10b), because of the removal of the inline surface waves after the f-k filtering.  
271 However, the performance of the f-k filtering in suppressing the horizontal arrivals is not  
272 good enough, as can be seen in Figure 10b, which leads to a large amount of those  
273 horizontal arrivals still remaining. On the contrary, those horizontal arrivals, along with  
274 inline surface waves, are significantly reduced in Figure 10c, leading to the emergence of  
275 two clear reflections (red arrows in Figure 10c).

276 Figure 11a is the stacked section obtained from the original data (containing the  
277 source-coherent and source-incoherent surface waves). Figures 11b and 11c show the  
278 stacked sections obtained from the same data after suppression of these two types of  
279 surface waves using f-k filtering and SI+AS schemes, respectively. The events (e.g., red  
280 rectangle in Figure 11a), caused by the stacking of source-incoherent surface-wave  
281 arrivals, can be wrongly interpreted as reflectors because of their continuity and clarity,  
282 which would be really problematic in urban seismic surveys. As visible in Figure 11b,  
283 the f-k filtering fails to suppress these artefacts sufficiently (e.g., red rectangle in Figure  
284 11b) due to poor performance to suppress these horizontal arrivals without damaging the  
285 reflections. However, such artefacts are greatly reduced in Figure 11c – the reflectors are  
286 now correctly imaged and clearly interpretable. This shows that our approach is  
287 successful in the removal of most of the inline and crossline surface waves, with very  
288 little loss of the useful reflection energy.

289

### 290 **Modelling study 3: suppression of source-coherent surface waves and** 291 **dipping LMON**

292 Often, there are other types of noise sources (than what has been discussed above) in  
293 urban environments, such as construction work taking place around the survey line.

294 Crossline surface waves caused by these sources may be characterized by dipping  
295 moveouts. To test if the surface-wave-suppression scheme that we propose in modelling  
296 study 2 could help also in the suppression of dipping crossline surface waves, we add  
297 source-incoherent dipping arrivals to our previously modelled data (modelling study 1).  
298 A resulting common-source gather is shown in Figure 12a, where the dipping surface-  
299 wave arrivals are marked by blue arrows. We first try to use f-k filtering to suppress the  
300 inline surface waves and dipping arrivals in Figure 12a, which produces the result shown  
301 in Figure 13b. In the f-k domain, these dipping arrivals fall inside the area where also  
302 most of reflection energy is located. To suppress these dipping arrivals using f-k filtering  
303 will also mean total loss of reflection energy, as can be seen in Figure 13b.

304 To reveal the true reflections, we apply an SI+AS scheme (as illustrated in Figure  
305 12) similar to the one we used in the modelling study 2. The final common-source gather  
306 resulting from this scheme is displayed in Figure 13c. Two reflection events (red arrows  
307 in Figure 13c) have been revealed by the SI+AS procedure, and they can now be identified.  
308 Comparing the result in Figure 13c with the reference result shown in Figure 13d, we  
309 notice that the amplitudes of the revealed reflections in Figure 13c have been greatly  
310 weakened after the SI+AS procedure; nevertheless, they can be well-utilized in near-  
311 surface imaging.

312 Figure 14a shows the CMP stacked section using the data without surface-wave  
313 suppression. Two features (see the red rectangle in Figure 14a) with high amplitude and  
314 good continuity can be wrongly interpreted as reflectors. These features are due to the  
315 stacking of the dipping surface waves. These artefacts can be utterly misleading in the  
316 urban geophysical interpretation. Figure 14b shows the stacked section from the data after  
317 surface-wave suppression using f-k filtering. Because of the failure of the f-k filter to

318 suppress the dipping arrivals, artefacts (see the red rectangle in Figure 14b) caused by  
319 stacking these arrivals still remain in Figure 14b. The stacked section after surface-wave  
320 suppression using the SI+AS is shown in Figure 14c. Due to successful suppression of  
321 the dipping surface waves, the artefacts (e.g., red rectangle in Figure 14a) have nearly  
322 disappeared from Figure 14c. Therefore, we can now easily and correctly interpret the  
323 two deeper reflectors in Figure 14c.

324

### 325 **Field-data example**

326 In a high-resolution shear-wave reflection survey, the receiver line consisted of 120  
327 horizontal-component geophones spaced at a 0.25 m interval, ranging from 42 to 71.75m.  
328 The geophones were oriented in the crossline direction. The receiver array was fixed  
329 during data collection, because of the limited available space in the survey area, which is  
330 a common constraint in urban settings. As a source, we used a high-frequency,  
331 electrodynamic horizontal vibrator (Ghose *et al.* 1996; Brouwer *et al.* 1997; Ghose and  
332 Goudswaard 2004; Ghose 2012) also oriented in the crossline direction. The source  
333 spacing was 1 m, starting from 42 m to 62m. As both the sources and the receivers are  
334 oriented in the crossline direction, we made use of shear-waves polarized in the crossline  
335 direction, i.e., SH-waves. The record length was 4 s. After vibroseis source signature  
336 deconvolution (Ghose 2002), we obtain common-source gathers with a length of 0.5 s.  
337 Figure 15a shows an example common-source gather after application of AGC (180 ms)  
338 and band-pass filtering (3-8-150-200 Hz). During the field work, due to the surface  
339 condition and source coupling, unfortunately harmonic distortion was significant in the  
340 compressed vibrator data, which showed up as LMON (blue ellipse in Figure 15a). This  
341 kind of noise, together with the source-coherent surface waves, is difficult to suppress

342 using traditional filtering techniques (e.g., f-k filtering, notch filtering), due to the very  
343 similar frequency content and moveout velocity as the informative reflection signals. This  
344 makes this dataset ideal for testing the efficacy of our newly developed scheme.

345 In order to restore the true reflectors from this severely noise-contaminated data,  
346 we apply the SI+AS scheme, as illustrated in modelling study 3, to the data shown in  
347 Figure 15a, with the main aim to suppress the dipping arrivals (see the area inside the  
348 blue ellipse). The result is shown in Figure 15c. Comparing the common-source gathers  
349 in Figure 15a and 15c, we can see that the dipping arrivals are significantly suppressed,  
350 and shallow reflections around 100 ms can now be identified clearly in Figure 15c. We  
351 interpret them as true reflections because they are crisp and they also show clear  
352 hyperbolic moveouts in shot gathers. For the same gather, after f-k filtering (Figure 15b)  
353 it is difficult to identify such shallow reflection events.

354 Figure 15d, 15e, 15f present the stacked section from the raw (unfiltered) field  
355 data, data after f-k filtering, and data after SI+AS, respectively. In Figure 15e, we see that  
356 there are many artefacts (example marked by red rectangle) caused by the f-k filtering.  
357 Without prior knowledge about the subsurface, the interpretation can become erroneous.  
358 However, in Figure 15f we can interpret a shallow reflector at around 100 ms two-way  
359 time, with a vertical resolution of less than 1m, because of the good quality stacking. This  
360 is due to the success of SI+AS scheme in suppressing LMON, while preserving the  
361 shallow shear-wave reflections.

362

## 363 **Conclusions**

364 High-resolution reflection seismics using shear waves can be very effective in subsurface  
365 investigations in densely populated soil-covered urban settings. However, a successful

366 application of the method can be hampered by the presence of source-coherent surface  
367 waves and/or other LMON in the field data, which camouflage the shallow shear-wave  
368 reflection events. We developed new schemes for the data-driven suppression of such  
369 surface- wave noise and LMON, while preserving the shallow reflections. Using  
370 numerical modelling data, we showed how a combination of SI and AS can significantly  
371 suppress the inline (source-coherent) surface waves and LMON and, hence, improve  
372 significantly the imaging of shallow subsurface structures. In comparison with f-k  
373 filtering, we demonstrate that our schemes are effective in separating reflections from  
374 source-coherent surface waves and LMON, even when they overlap greatly in the f-k  
375 domain. When applied to field shear-wave reflection data that are heavily contaminated  
376 by LMON, we found that crisp and clear shallow reflectors could be revealed, due to  
377 significant suppression of LMON as a result of the application of the newly developed SI  
378 + AS schemes.

379

## 380 **ACKNOWLEDGEMENTS**

381 The research of J.L. is supported by the China Scholarship Council (File No.  
382 201604910851). The field data were acquired with the help of Dominique Ngan-Tillard,  
383 Joeri Brackenhoff, and Jens van den Berg. The seismic data were processed using a  
384 combination of Seismic Unix, ProMAX and software from the Delphi Consortium. The  
385 authors would like to thank the associate editor and two anonymous reviewers for their  
386 constructive comments that helped improve the manuscript.

387

388

389

390 **References**

- 391 Bekara M. and van der Baan M. 2007. Local singular value decomposition for signal  
392 enhancement of seismic data. *Geophysics* **72**, V59–V65.
- 393 Brouwer J., Ghose R., Helbig K. and Nijhof V. 1997. The improvement of geotechnical  
394 subsurface models through the application of S-wave reflection seismic exploration.  
395 *Proc. 3<sup>rd</sup> Environ. Engineering Geophys. Soc Europ. Section Meeting*, 103-106.
- 396 Dong S., He R. and Schuster G. 2006. Interferometric prediction and least squares  
397 subtraction of surface waves. *SEG Technical Program Expanded Abstracts*. **2006**,  
398 pp. 2783–2786.
- 399 Draganov D., Heller K. and Ghose R. 2012. Monitoring CO<sub>2</sub> storage using ghost  
400 reflections retrieved from seismic interferometry. *International Journal of*  
401 *Greenhouse Gas Control* **11**, S35–S46, doi: 10.1016/j.ijggc.2012.07.026.
- 402 Draganov D., Ghose R., Heller K. and Ruigrok E. 2013. Monitoring of changes in  
403 velocity and Q in reservoirs using non-physical arrivals in seismic interferometry.  
404 *Geophysical Journal International* **192**, 699-709, doi: 10.1093/gji/ggs037.
- 405 Eckart C. and Young G. 1936. The approximation of one matrix by another of lower rank.  
406 *Psychometrika* **1**, 211–218.
- 407 Ghose R., Brouwer J. and Nijhof V. 1996. A portable S-wave vibrator for high-resolution  
408 imaging of the shallow subsurface. 58th EAGE Conference and Exhibition.
- 409 Ghose R., Nijhof V., Brouwer J., Matsubara Y., Kaida Y. and Takahashi T. 1998.  
410 Shallow to very shallow, high-resolution reflection seismic using a portable vibrator  
411 system. *Geophysics* **63**, 1295–1309.
- 412 Ghose R. 2002. High-frequency shear wave reflections from shallow subsoil layers using  
413 a vibrator source; sweep cross-correlation versus deconvolution with groundforce

414 derivative. *72<sup>nd</sup> Annual International Meeting, SEG, Expanded Abstracts*, pp. 1408-  
415 1411.

416 Ghose R. and Goudswaard J. 2004. Integrating S-wave seismic-reflection data and cone  
417 penetration test data using a multiangle multiscale approach. *Geophysics* **69**, 440-  
418 459.

419 Ghose R. 2012. A microelectromechanical system digital 3C array seismic cone  
420 penetrometer. *Geophysics* **77**, WA99-WA107.

421 Golub G. and van Loan C. 1996. *Matrix Computations*, The Johns Hopkins Univ. Press,  
422 Baltimore, MD.

423 Guitton A. and Verschuur D.J. 2004. Adaptive subtraction of multiples using the L1-  
424 norm. *Geophys. Prospect.* **52**, 27-38.

425 Halliday D., Curtis A., Robertsson J. and van Manen D. 2007. Interferometric surface-  
426 wave isolation and removal. *Geophysics* **72**, A69-A73.

427 Hasbrouck W. P. 1991. Four shallow-depth, shear-wave feasibility studies. *Geophysics*  
428 **56**, 1875-1885.

429 Haworth R.J. 2003. The shaping of Sydney by its urban geology. *Quaternary*  
430 *International* **103**, 41-55.

431 King S. and Curtis A. 2012. Suppressing nonphysical reflections in Green's function  
432 estimates using source-receiver interferometry. *Geophysics* **77**, Q15-Q25, doi:  
433 10.1190/geo2011-0300.1.

434 Konstantaki L.A., Ghose R., Draganov D., Diaferia G. and Heimovaara T. 2014.  
435 Characterization of a heterogeneous landfill using seismic and electrical resistivity  
436 data. *Geophysics* **80**, EN13-EN25.

437 Konstantaki L.A., Draganov D., Ghose R. and Heimovaara T. 2015. Seismic

438 interferometry as a tool for improved imaging of the heterogeneities in the body of  
439 a landfill. *Journal of Applied Geophysics* **122**, 28–39.

440 Krawczyk C., Polom U. and Beilecke T. 2013. Shear-wave reflection seismics as a  
441 valuable tool for near-surface urban applications. *The Leading Edge* **32**, 256–263.

442 Melo G., Malcolm A., Mikesell T.D. and van Wijk K. 2013. Using SVD for improved  
443 interferometric green's function retrieval, *Geophys. J. Int.* **194**(3), 1596–1612.

444 Mikesell D., van Wijk K., Calvert A. and Haney M. 2009. Virtual refraction: Useful  
445 spurious energy in seismic interferometry. *Geophysics* **74**, A13–A17, doi:  
446 10.1190/1.3095659.

447 Pugin A., Larson T., Sargent S., McBride J. and Bexfield C. 2004. Near-surface mapping  
448 using SH-wave and P-wave seismic land-streamer data acquisition in Illinois, U.S.  
449 *The Leading Edge* **23**, 677–682.

450 Pullan S. E., Hunter J. A. and Neave K. G. 1990. Shallow shear-wave reflection tests, 60<sup>th</sup>  
451 Ann. Internat. Mtg., Soc. Expl. Geophys., Expanded Abstracts, 380-382,

452 Sinsakul S. 2000. Late Quaternary geology of the Lower Central Plain, Thailand. *Journal*  
453 *of Asian Earth Sciences* **18**, 415–426.

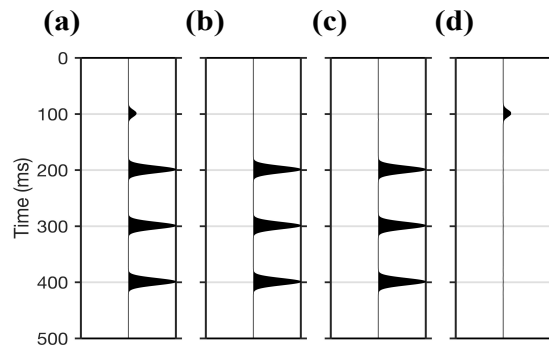
454 Snieder R. 2004. Extracting the Green's function from the correlation of coda waves: A  
455 derivation based on stationary phase. *Physical Review E* **69**, 46610.

456 Thorbecke J. and Draganov D. 2011. Finite-difference modeling experiments for seismic  
457 interferometry. *Geophysics* **76**, H1–H18.

458 Wapenaar K. and Fokkema J. 2006 Green's function representations for seismic  
459 interferometry. *Geophysics* **71**, SI33–SI46, doi: 10.1190/1.2213955.

460 Yilmaz Ö. 2001. Seismic data analysis: processing, inversion and interpretation of  
461 seismic data: SEG, USA.

462



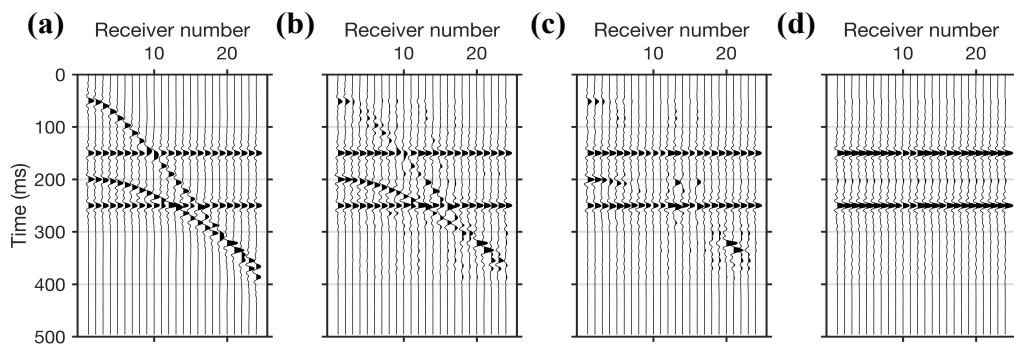
463

464 Figure 1: Illustration of the basic steps involved in adaptive subtraction (AS): (a)  $\mathbf{D}$  is

465 seismic data with one weak reflection and three high-amplitude surface waves; (b)  $\mathbf{D}^{sw}$  is

466 the surface-waves part of Figure 1a; (c)  $\mathbf{fD}^{sw}$  results from convoluting the estimated

467 shaping filter  $\mathbf{f}$  with Figure 1b; (d)  $\mathbf{D}^{refl}$  is data after surface-waves suppression.



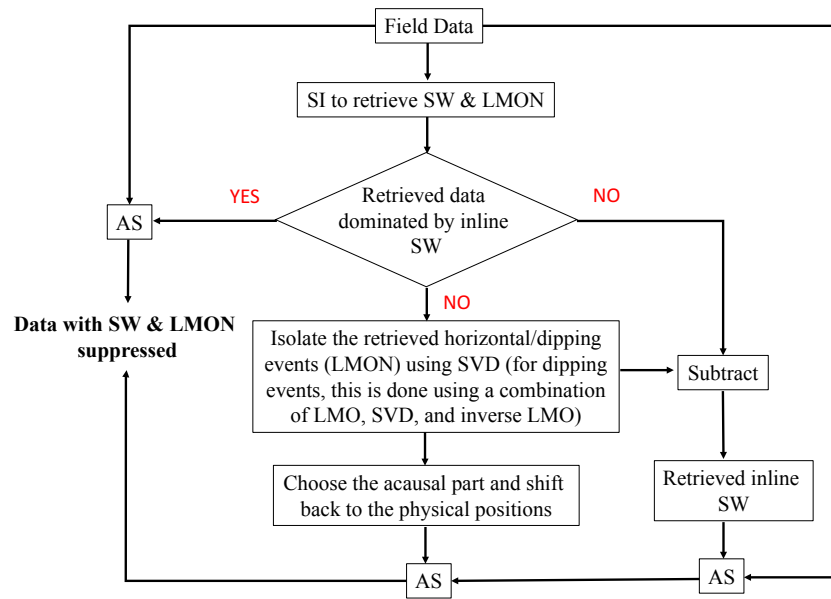
468

469 Figure 2: Illustration of the steps necessary to isolate horizontal arrivals from the seismic

470 reflection shot gather using singular value decomposition (SVD) filtering: (a) synthetic

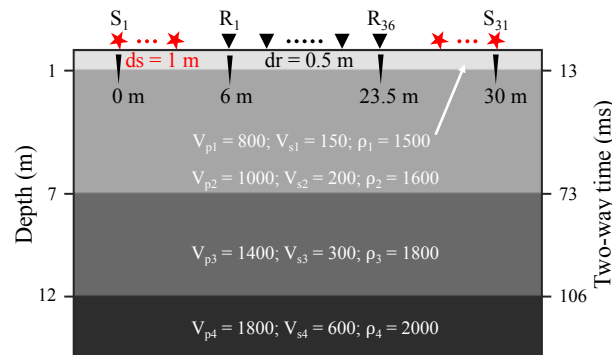
471 seismic data (representing matrix  $\mathbf{C}$ ) with two horizontal noise events; (b-d) the low-rank

472 matrix  $\mathbf{C}_j$  of  $\mathbf{C}$ , by setting  $j$  to 12, 6, and 2, respectively.



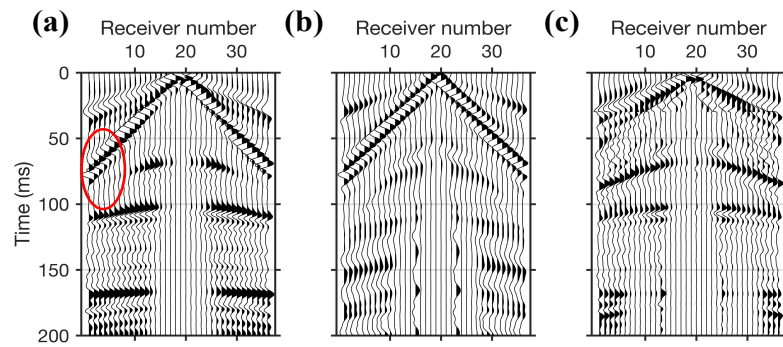
473

474 Figure 3: Flowchart for the implementation of seismic interferometry and adaptive  
 475 subtraction (SI+AS) schemes to suppress source-coherent surface waves (SW) and linear  
 476 moveout noises (LMON).



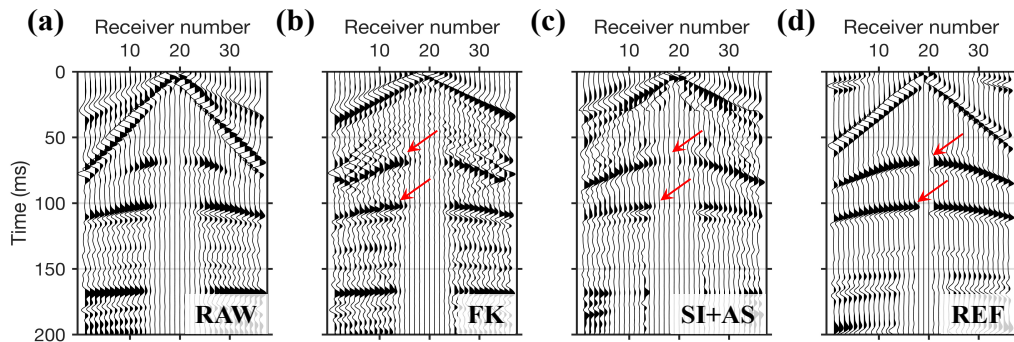
477

478 Figure 4: Model used to generate synthetic shot gathers. The units for  $V_p$ ,  $V_s$ , and  $\rho$  are  
 479 m/s, m/s, and  $\text{kg/m}^3$ , respectively. The acquisition geometry used for the synthetic studies  
 480 is illustrated at the top of the model. The red stars represent sources, while the black  
 481 triangles are receivers. The depth of each interface and its corresponding shear-wave  
 482 reflection two-way time, are shown on left and right vertical axis, respectively.



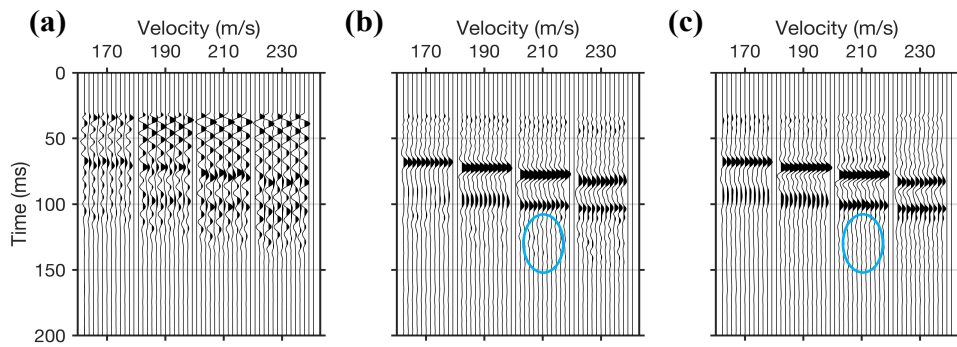
483

484 Figure 5: Steps for the implementation of the SI+AS scheme to suppress source-coherent  
 485 surface waves: (a) a synthetic shot gather from the source located at 15 m; (b) retrieved  
 486 virtual common-source gather using SI, with virtual source positioned at 15 m; (c) result  
 487 after AS of the data in Figure 5b from the data in Figure 5a. The red ellipse highlights the  
 488 area where the surface waves overlaps the reflection. For a better visualisation of events,  
 489 an automatic gain control (AGC) with a window length of 50 ms is applied to the shot  
 490 gathers. This same AGC is also applied to all other synthetic shot gathers presented in the  
 491 following illustrations.



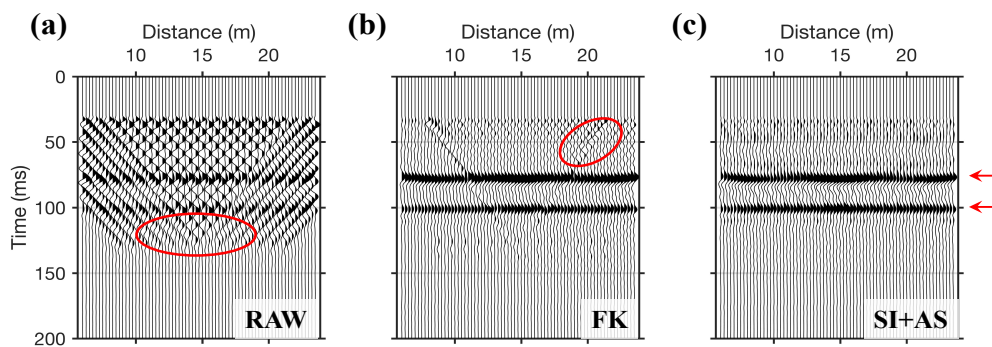
492

493 Figure 6: Comparison between the shot gather as in Figure 5a and the results after the  
 494 application of f-k filtering and after SI+AS: (a) raw data as in Figure 5a; (b) result after  
 495 f-k filtering; (c) result after SI+AS; (d) corresponding reference gather modelled without  
 496 surface wave. The red arrows mark the primary shear-wave reflections from the interfaces  
 497 of the model (at depth 7 m and 12 m), shown in Figure 4.



498

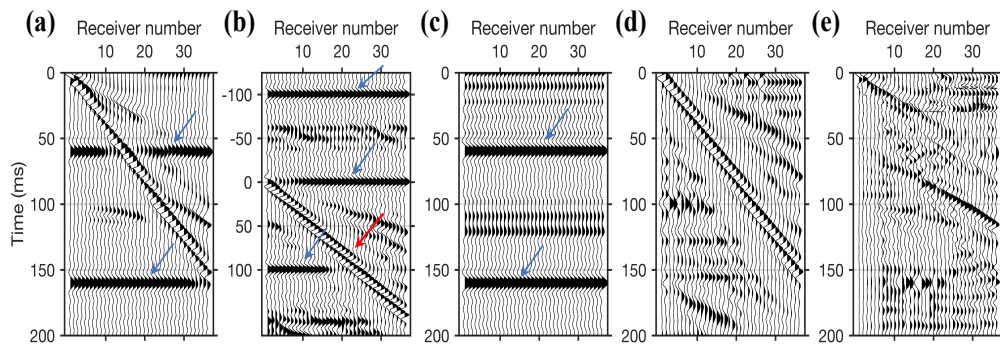
499 Figure 7: Comparison between constant velocity stacks (CVSs) from the raw data, data  
 500 after f-k filtering, and data after SI+AS: (a) CVS section from the data as in Figure 6a  
 501 without removal of surface waves; (b) CVS section after f-k filtering; (c) CVS section  
 502 after SI+AS. For the CVS sections (e.g., Figure 7a), each subpanel shows a part of the  
 503 stacked section, located from 14 m to 16.5 m in the model, obtained from stacking with  
 504 different velocity labelled above the x-axis. The CVS sections (also the stacked sections  
 505 in the following synthetic studies) are displayed without AGC, but after top muting the  
 506 part above 30 ms. The blue ellipse highlights noise in Figure 7b that has a higher amplitude  
 507 than in Figure 7c.



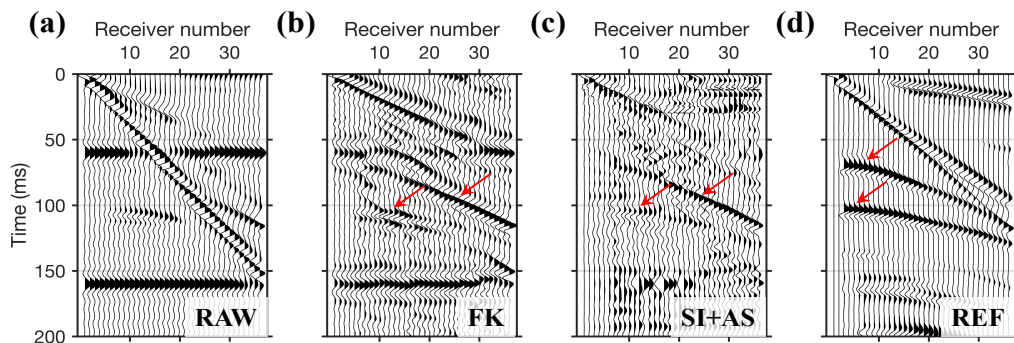
508

509 Figure 8: Comparison between stacked sections (located from 6 m to 23.5 m), from the  
 510 raw data, data after f-k filtering, and data after SI+AS: (a) stacked section from data as in  
 511 Figure 6a without removal of surface waves; (b) stacked section after f-k filtering; (c)  
 512 stacked section after SI+AS. The areas highlighted by red ellipses are caused by stacking

513 of surface waves. We indicate the theoretical shear-wave two-way time from the second  
 514 and third reflectors of the model in Figure 4 with red arrows on the right side of the panels.

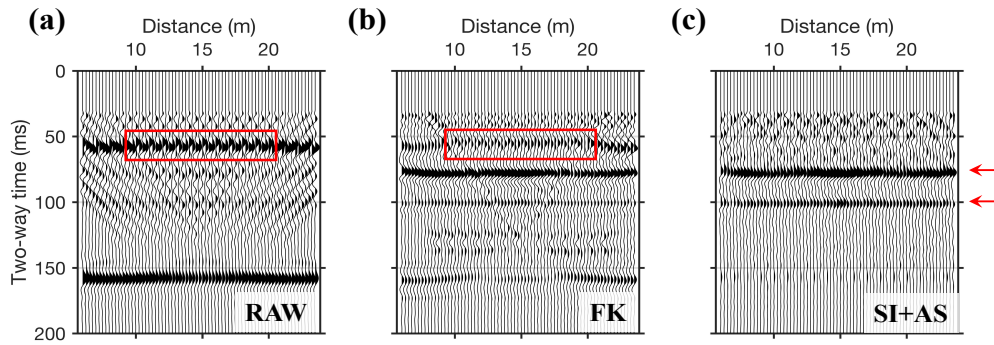


515  
 516 Figure 9: Steps for the implementation of the SI+AS to suppress source-coherent surface  
 517 waves and horizontal linear moveout noises (LMON): (a) a synthetic shot gather for a  
 518 source located at 6 m, where the blue arrows mark the horizontal LMON; (b) retrieved  
 519 virtual common-source gather using SI for a virtual source located at 6 m, where the blue  
 520 and red arrows indicate the retrieved horizontal LMON and the retrieved inline surface  
 521 waves, respectively; (c) retrieved horizontal arrivals that are isolated using SVD and then  
 522 manually moved to the time of the corresponding events in Figure 9a; (d) retrieved inline  
 523 surface waves extracted from Figure 9b through subtraction of the retrieved horizontal  
 524 LMON; (e) result after AS of the data in Figure 9c and Figure 9d from the data in Figure  
 525 9a.



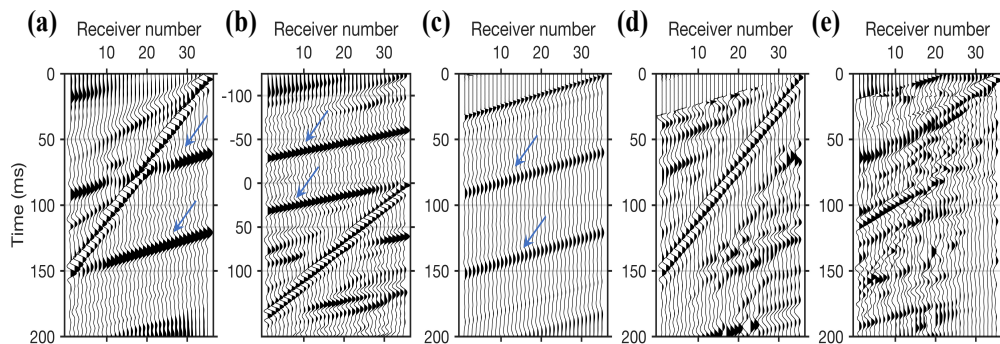
526

527 Figure 10: As in Figure 6, but in case of suppression of both source-coherent surface  
 528 waves and horizontal linear moveout noises. The red arrows indicate the reflections from  
 529 the interfaces of the model (Figure 4) at depths of 7 m and 12 m.



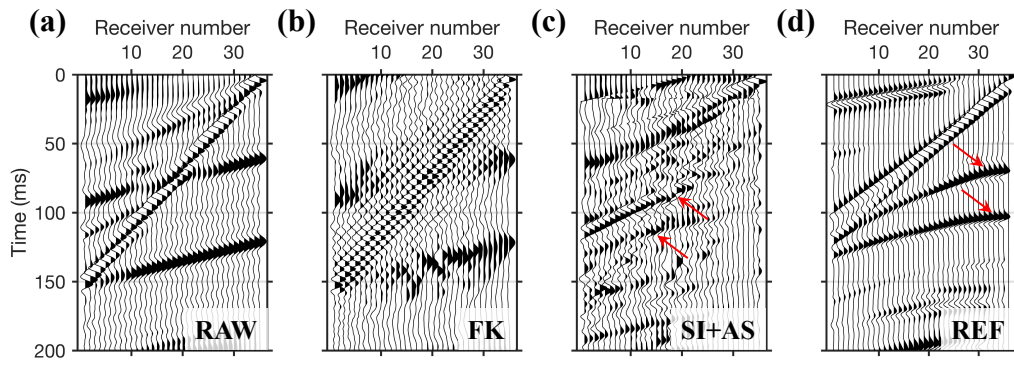
530

531 Figure 11: As in Figure 8, but for the data with source-coherent surface waves and  
 532 horizontal linear moveout noises (LMON). Red rectangles mark the artefacts caused by  
 533 stacking LMON.



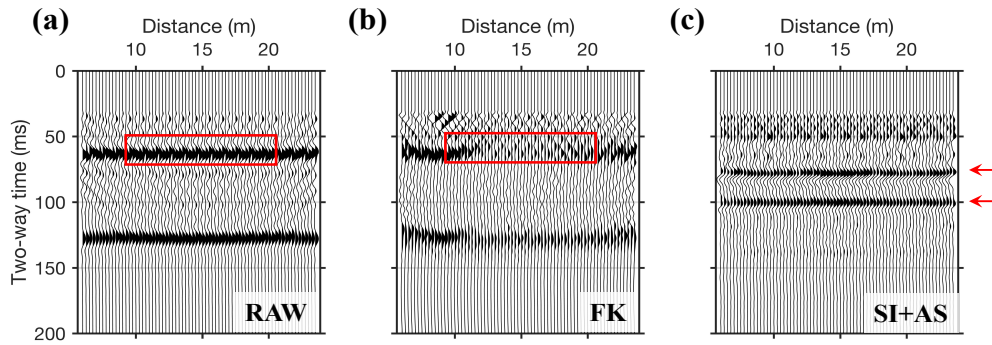
534

535 Figure 12: As in Figure 9, but in case of suppression of both source-coherent surface  
 536 waves and dipping linear moveout noises (LMON). The active and virtual shot are at 24  
 537 m.



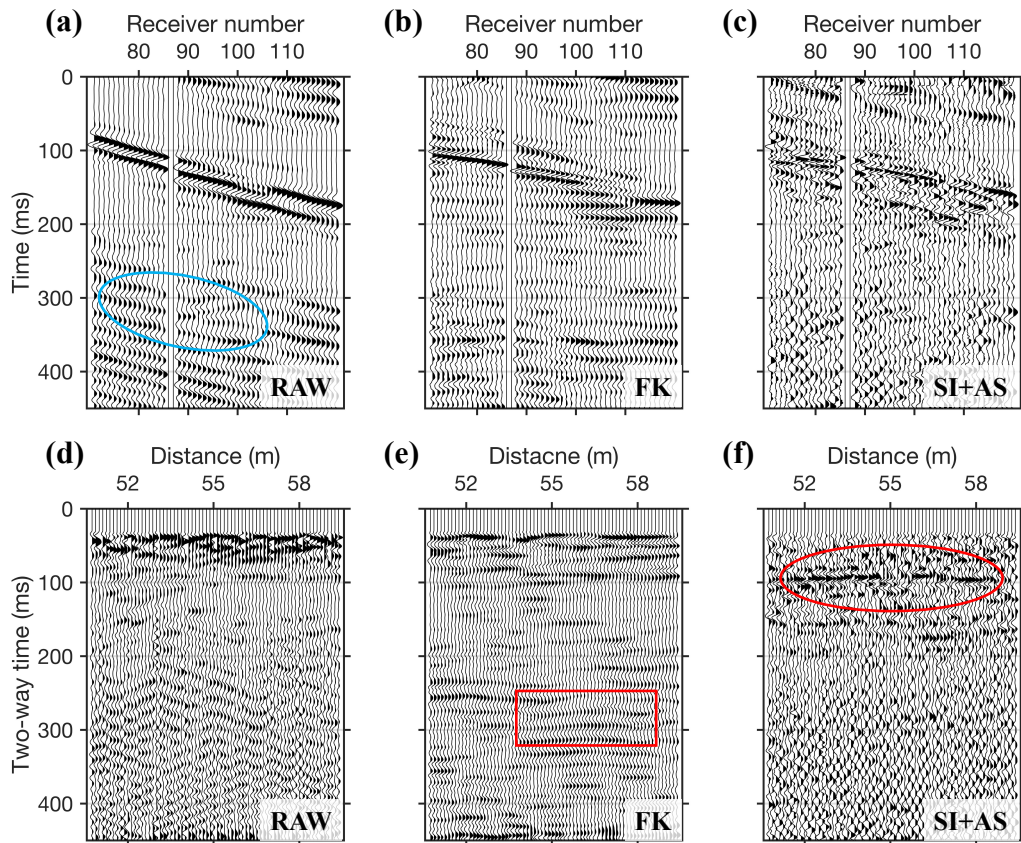
538

539 Figure 13: As in Figure 10, but in case of suppression of both source-coherent surface  
 540 waves and dipping linear moveout noises (LMON). The active and virtual shots are at 24  
 541 m.



542

543 Figure 14: As in Figure 11, but for the data with source-coherent surface waves and  
 544 dipping linear moveout noises (LMON).



545

546 Figure 15: Comparison between field shear-wave shot gathers: (a) a typical raw shear-  
 547 wave shot gather acquired in the field contaminated by dipping linear moveout noises  
 548 (blue ellipse), with the source located at 50 m; (b) result after careful f-k filtering; (c)  
 549 result after SI+AS, following the procedure outlined in Figure 3. Comparison between  
 550 field shear-wave stacked sections: (d) using raw (unfiltered) field data; (e) using f-k  
 551 filtered data; (f) using SI+AS data. The red rectangle highlights the artefacts caused by f-  
 552 k filtering, whereas the red ellipse marks the revealed shallow reflectors via SI+AS.